Enhanced Thermal Transport across Self-Interfacing van der Waals Contacts in Flexible Thermal Devices

Minho Seong, Insol Hwang, Seongjin Park, Hyejin Jang, Geonjun Choi, Jaeil Kim, Shin-Kwan Kim, Gun-Ho Kim, Junyeob Yeo, and Hoon Eui Jeong*

Minimizing the thermal contact resistance (TCR) at the boundary between two bodies in contact is critical in diverse thermal transport devices. Conventional thermal contact methods have several limitations, such as high TCR, low interfacial adhesion, a requirement for high external pressure, and low optical transparency. Here, a self-interfacing flexible thermal device (STD) that can form robust van der Waals mechanical contact and low-resistant thermal contact to planar and non-planar substrates without the need for external pressure or surface modification is presented. The device is based on a distinctive integration of a bioinspired adhesive architecture and a thermal transport layer formed from percolating silver nanowire (AgNW) networks. The proposed device exhibits a strong attachment (maximum 538.9 kPa) to target substrates while facilitating thermal transport across the contact interface with low TCR (0.012 m² K kW⁻¹) without the use of external pressure, thermal interfacial materials, or surface chemistries.

1. Introduction

An interface, which is a boundary between two different bodies in contact, causes resistance to heat flow across the bodies.[1] The heat flux (q) across the contact interface is directly related to the thermal contact resistance (TCR) for a given temperature gradient (ΔT) by Fourier's law: $q = \Delta T/R_{tc} = G\Delta T$.[2] Here, R_{tc} and G represent the TCR and the interfacial thermal conductance, respectively. Minimizing the TCR is a critical requirement that has implications for the performance, power efficiency, and reliability of most thermal transport devices,[3] including heaters and coolers.[4]

M. Seong, I. Hwang, S. Park, H. Jang, G. Choi, J. Kim, S.-K. Kim,
G.-H. Kim, H. E. Jeong
Department of Mechanical Engineering
Ulsan National Institute of Science and Technology (UNIST)
Ulsan 44919, Republic of Korea
E-mail: hoonejeong@unist.ac.kr
J. Yeo
Department of Physics
Kyungpook National University
Daegu 41566, Republic of Korea

The ORCID identification number(s) for the author(s) of this article can be found under https://doi.org/10.1002/adfm.202107023.

The interfacial thermal resistance can be reduced by enhancing the interfacial bond or adhesion strength.[5] Previous studies have demonstrated that the formation of strong covalent bonds at the interfaces by surface chemistry through the use of self-assembled monolayers (SAMs) can significantly enhance interfacial thermal transport.[2b,6] However, such an approach is usually not appropriate for actual device applications because the interface in a device is generally formed through physical means rather than through chemical reactions with the use of additional chemicals.[7] In addition, the formation of chemical bonds is only effective for particular substrates.[8] Furthermore, chemical bond formation essentially requires continuous and close mechanical contact at the interface so that the two bodies are sufficiently close to each other.[9] However, in reality, when surfaces come into contact, interfacial roughness due to micro- and nano-scale asperities hinders intimate mechanical and thermal contact and results in the reduction of the actual contact area and the formation of air gaps with poor thermal conductivity.[10]

Thus, it is highly desirable to create intimate mechanical contact based on van der Waals (vdW) interactions to reduce the TCR at the interface.[11] Conventionally, close mechanical coupling is achieved by applying an external load.[12] Gotsmann et al. showed that increasing the applied external load increases the number of contact points and the actual contact area, thereby reducing the TCR by providing extra channels for heat transfer.[10b] This result has the implication that the formation of stable mechanical contacts at interfaces can be an important route for enhancing interfacial thermal transport. However, the prolonged application of external high loads to thermal devices is neither easy nor practical for actual applications. Thermal interface materials (TIMs) with high thermal conductivity are often applied to interfaces to reduce interfacial thermal resistance in many thermal applications.[4d,13] However, TIMs also have several disadvantages, such as relatively low thermal performance, optical transparency, and interfacial adhesion and high viscous fluidity, and their residues cause contamination.[14] These disadvantages limit their application in recently emerging flexible thermal devices (e.g., flexible transparent heaters), in which precise and accurate contact interfaces, mechanical flexibility, optical transparency, and superior thermal properties are prerequisite requirements.[15]

Herein, we present a self-interfacing flexible thermal device (STD) that can significantly enhance interfacial thermal

transport by maximizing mechanical vdW coupling without the application of external pressure or surface chemistry. The device is composed of two crucial components, namely, a bioinspired adhesive architecture for intimate and immediate mechanical coupling, and a silver nanowire (AgNW) percolating network for efficient heat flow. The distinctive design of the device allows it to form strong mechanical adhesive and low-resistant thermal contact with planar and nonplanar substrates without the need for external loads or surface modification. The device is also highly flexible and transparent; thus, it can be utilized as a self-interfacing flexible transparent heater. We demonstrate the reduction of the TCR by approximately 97% on flat substrates and approximately 96% on rough substrates without external pressure by the device compared to a conventional non-structured flexible thermal device (NTD), even under a large applied pressure of 100 kPa.

2. Results and Discussion

2.1. Design and Fabrication of the Self-Interfacing Flexible Thermal Device

Figure 1 shows a conceptual illustration of the STD proposed in this study. The device consists of two main components,

namely, a self-interfacing adhesive architecture and thermal transport layers of percolating AgNW networks (Figure 1A). The adhesive architecture has two structural components comprising a regular grid and micropillars with extruded tips. The grid pattern forms the main framework of the device. The thermal and optical properties of the device can be modulated by controlling the geometry of the framework. However, the grid pattern by itself does not exhibit robust mechanical adhesion to the contacting substrates. We therefore endow the grid pattern with a strong mechanical adhesion capability by integrating an adhesive architecture of protruding tips along with the grid pattern (Figure 1A). Previous studies have shown that microstructures with protruding tips found in living creatures such as geckos and beetles are crucial in enhancing vdW-based mechanical adhesion by evenly distributing the contact stress at the interfaces.[16] Thus, the grid pattern with protruding wing tips along the sidewall exhibits enhanced mechanical adhesion. In addition to the grid with tips, we also integrated a micropillar array with protruding tips between the grid pattern to further strengthen the mechanical coupling of the thermal device with the substrate. AgNWs are selectively deposited along the grid pattern to form thermally conductive percolating networks across the entire surface of the STD. Note that the AgNWs are not deposited in the tip regions of the grid. For efficient heat
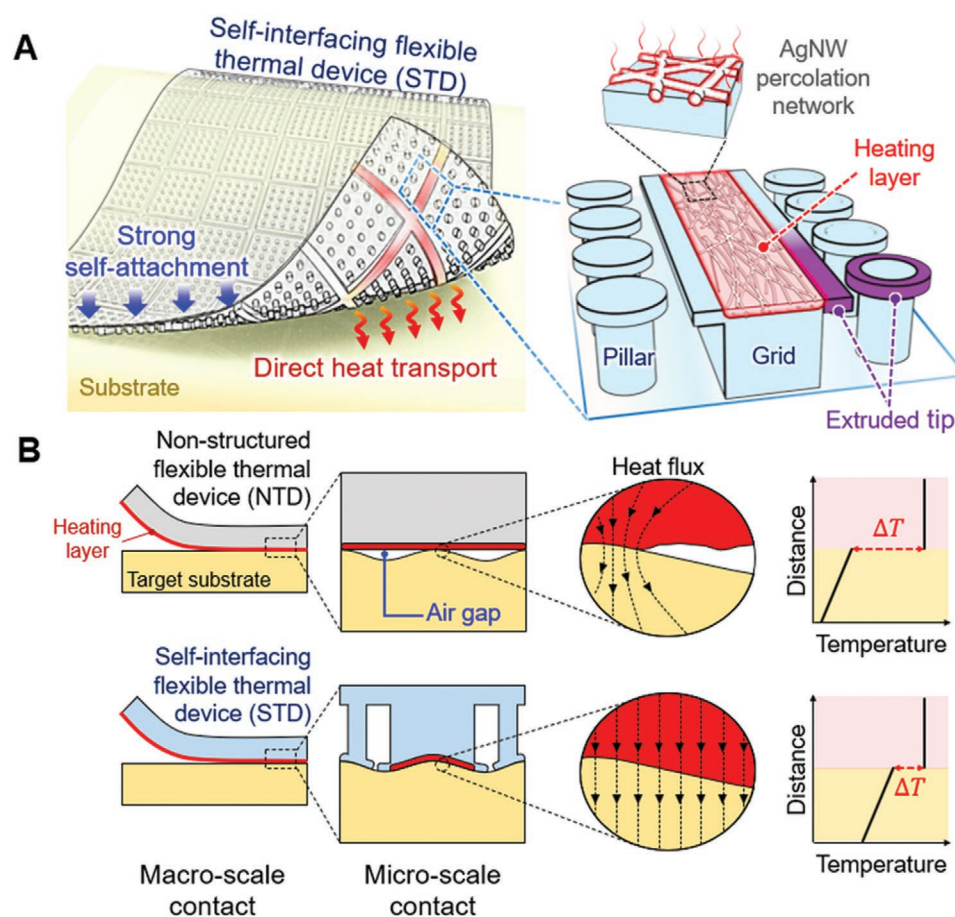
Figure 1. Design of self-interfacing flexible thermal device. A) Conceptual illustration showing the structure of the self-interfacing flexible thermal device. B) Thermal contact mechanisms of the non-structured (upper) and the self-interfacing flexible thermal devices (bottom).

generation and direct heat transport across the contact interfaces, the heating layer of the STD should have high electrical and thermal conductivity. AgNWs have a superior electrical conductivity of 5×10^7–2×10^8 S m^{-1} compared to other conductive nanomaterials such as carbon nanotubes (2×10^3–1×10^5 S m^{-1}) and graphene (8×10^4–6×10^5 S m^{-1}).[17] Although the thermal conductivity of AgNWs (300–400 W m^{-1} K^{-1}) is lower than that of carbon nanotubes (500–3000 W m^{-1} K^{-1}) or graphene (1000–5000 W m^{-1} K^{-1}), AgNWs have the highest optical transmittance compared to others, making them an excellent candidate for an active layer of transparent flexible thermal devices.[17c,18]

This intriguing design allows the device to couple intimately to target substrates with strong mechanical vdW adhesion and minimize the TCR without using external loading forces or chemical adhesives. Figure 1B shows the thermal contact mechanisms of a flexible thermal device based on a non-structured planar surface in contact with the target substrate (top row), and that of a thermal device based on the self-interfacing microstructure (bottom row). When two planar surfaces come into contact, discrete and partial point contacts with air gaps are formed at the contact interfaces because the surfaces are not perfectly flat.[10b,19] The non-conformal point contacts and air gaps with low thermal conductivity decrease the thermal transport at the interface.[4d,20] The proposed STD design addresses this issue. The grid and pillar structures with extruding tips enable strong self-coupling with substrates, whereas the AgNW networks enable efficient thermal transport.
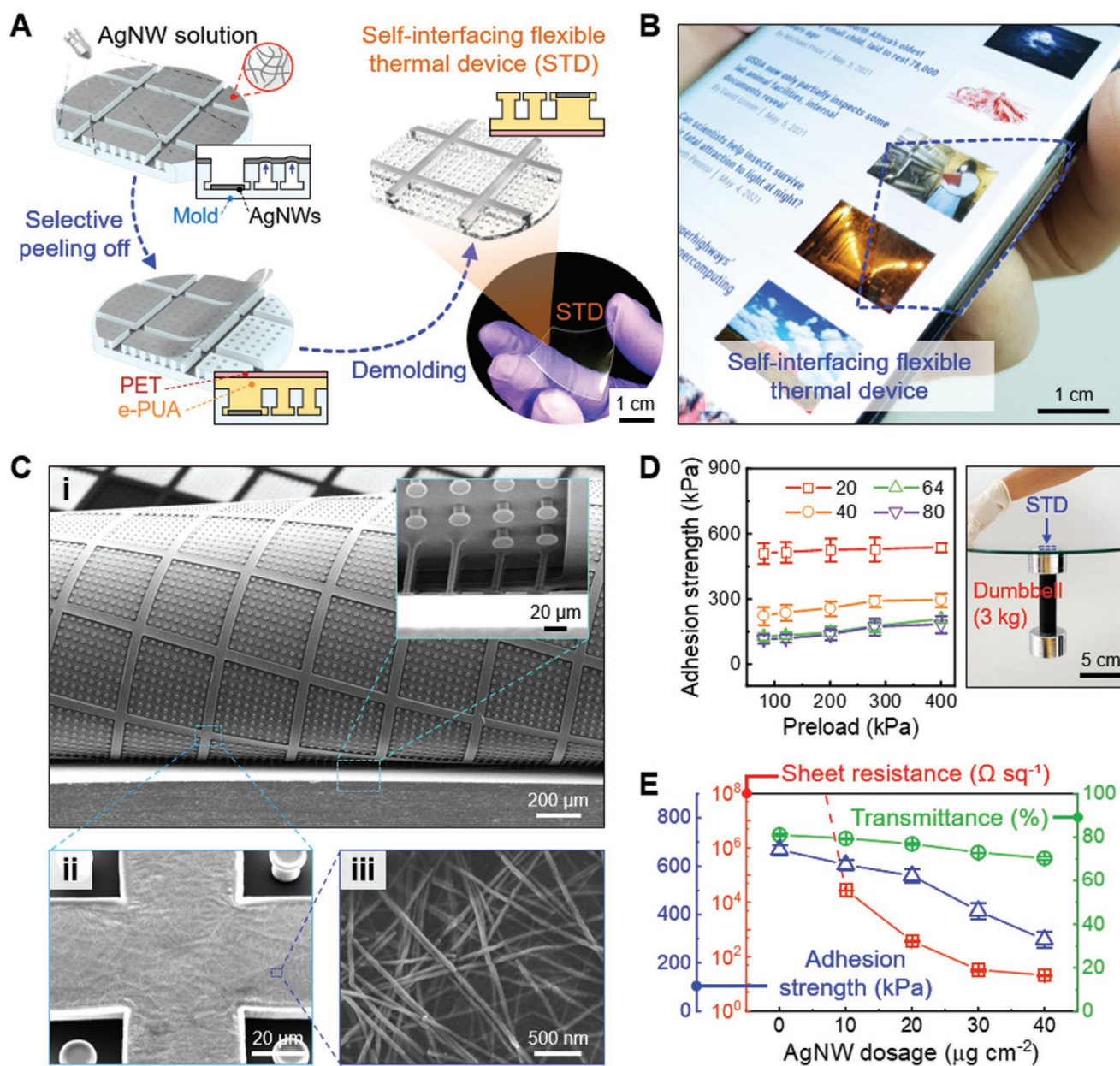
The STD was prepared by replica molding using a UV-curable resin and AgNW solution (see Figure S1 Supporting Information and the experimental section for details) (**Figure 2**A). First, a negative pattern of grids and micropillars with protruding tips was fabricated through a photolithographic process.[21] The AgNW solution was spray-coated onto the patterned mold. The AgNWs deposited outside of the negative pattern were selectively removed using adhesive tape, which resulted in selectively deposited AgNWs along the trenches of the grid. The AgNWs dispersed in the solution could not be deposited into the micropillar holes due to the high capillary pressure of the small-diameter holes, while the low capillary pressure of the grids having a large (effective) diameter allows the deposition of the AgNWs.[22] Also, the long length (20 μm) of the AgNWs hinders their deposition in the micropillar holes (diameter: 10 μm). Subsequently, UV-curable elastic polyurethane acrylate (e-PUA) was poured over the mold, followed by UV exposure. Removing the crosslinked e-PUA from the mold resulted in the STD with selectively embedded AgNW networks.

The resulting STD was highly flexible and transparent. Moreover, it could intimately and firmly adhere to a curved substrate, such as the edge of a smartphone (Figure 2B). Microscopical regular grid and pillar structures with wing tips were uniformly formed across the device, whereas the AgNW networks were selectively deposited over the grid structures (Figure 2C). The grid structures were 40 μm wide and had a center-to-center pitch of 400 μm (Figure S2, Supporting Information). The pillars had a stem diameter of 10 μm and center-to-center pitches of 20, 40, 64, or 80 μm, and both the grid and pillars were 15 μm high. The protruding tips of the grid and pillars were 2 μm long and 2 μm thick. AgNWs with an average diameter of 20 nm and a length of 20 μm were used to form AgNW networks

on top of the grid structure. AgNWs with larger diameters have higher electrical and thermal conductivity.[17c] However, AgNWs of larger diameters exhibit lower mechanical flexibility. Increasing the length or aspect ratio of AgNWs improves the connectivity of AgNWs in percolating networks.[15e] However, AgNWs with a high aspect ratio have low processability. In this study, the geometry of AgNWs was selected for the STD to have a low sheet resistance, high optical transmittance, high mechanical flexibility, and facile processability. Scanning electron microscopy (SEM) and energy dispersive spectroscopy (EDS) analysis verified that the AgNWs were selectively deposited only on the grid structure (Figure 2C -ii, -iii, and Figure S3, Supporting Information). In particular, the Ag in the AgNW percolation networks appeared only in the inner region of the top of the grid pattern; this therefore allowed the tip region of the grid to achieve mechanical adhesion to the target substrate. The AgNWs were also partially embedded in the grid structures (Figure 2C). The partially embedded AgNWs provide direct thermal contact of AgNWs with the target surface and also improve mechanical stability in a simultaneous manner.

The mechanical adhesion of the STD against a flat glass substrate was investigated as a function of the applied preload (80–400 kPa) and the pitch of the pillars (20, 40, 64, and 80 μm) (Figure 2D). The preload was removed during the adhesion measurements. Surprisingly, even under a relatively small preload of 80 kPa, the STD with a 20 μm pillar pitch exhibited the remarkable adhesion strength of 511.4 kPa (AgNW coating dosage: 40 μg cm^{-2}). Note that this adhesion strength value is significantly higher than the adhesion strength of planar PDMS (approximately 100 kPa) widely utilized in existing flexible thermal devices.[23] Devices with the pillar pitches of 40, 64, and 80 μm also showed fairly high adhesion strengths of 224.8, 128.2, and 116 kPa, respectively. The adhesion strengths increased slightly with the preload (Figure 2D) and saturated under a preload of 400 kPa. The saturated adhesion strengths of the devices with 20, 40, 64, and 80 μm pitch were 538.9, 297.0, 209.0, and 184.1 kPa, respectively. In contrast to the high level of adhesion of the STD, the maximum adhesion strength of the non-structured planar surface with the same coating dose of AgNWs (40 μg cm^{-2}) was only 30.3 kPa (preload: 400 kPa) (Figure S4, Supporting Information). The protruding tips of the micropillars and grid play a critical role in the adhesion enhancement of the STD, since the tips maximize the adhesion strengths by increasing the contact area and uniformly distributing stress at the contact interfaces. For example, the adhesion strength of the grid with protruding tips (211.2 kPa) is 85% higher than that of the grid without tips (114.2 kPa) (Figure S5, Supporting Information). The STD could maintain strong adhesion even at high temperatures up to 100 °C (Figure S6, Supporting Information). To evaluate the performance of the STD comprehensively, we measured the mechanical adhesion, sheet resistance, and optical transmittance as functions of the AgNW coating dose at the pillar pitch of 40 μm (Figure 2E). With an increase in the AgNW coating dose, the adhesion strength decreased to 606.1, 560, 415, and 297 kPa for the AgNW coating doses of 10, 20, 30, and 40 μg cm^{-2}, respectively (preload: 400 kPa, see also Figure S4, Supporting Information). The sheet resistance could also be adjusted from

**ADVANCED
SCIENCE NEWS**

www.advancedsciencenews.com

**ADVANCED
FUNCTIONAL
MATERIALS**

www.afm-journal.de

Figure 2. Fabrication of STD. A) Fabrication procedure of the STD. The inset shows the fabricated STD. B) Photograph of the flexible STD intimately attached to the curved edge of a smartphone. C) SEM images of the STD showing (i) the grid and micropillar structures, (ii) AgNWs that are selectively coated along the grid surfaces, and (iii) enlarged AgNWs. The inset image shows that the micropillars are highly elongated owing to their strong adhesion to the substrate. D) Adhesion strengths of the STD with four different pitches of pillars (20, 40, 64, and 80 µm) as functions of the preload for the fixed AgNW coating dose of 40 µg cm^{-2} (pulling rate of 1 mm s^{-1}). The image on the right side shows that the STD (area: 1×1 cm^2) can support a 3 kg dumbbell against a glass substrate. E) Adhesion strength, sheet resistance, and transmittance of the STD as functions of AgNW coating dose.

infinity to 21 Ω sq^{-1} by modulating the AgNW concentration. The transmittance ranged from 81% to 70% depending on the AgNW dose, showing a high level of transparency. The transmittance could be enhanced further at the cost of a small reduction in the adhesion strength by reducing the pillar density (Figure S7, Supporting Information). The adhesion, sheet resistance, and transmittance can be modulated by controlling the AgNW coating dose and dimension of the microstructures of the STD for specific applications.

2.2. Thermal Contact Resistance of the Self-Interfacing Flexible Thermal Device

To evaluate the thermal transport performance of the STD, we conducted TCR measurements using a steady-state method (**Figure 3**). The thermal device was first attached to a flat glass substrate (thickness: 0.17 mm) placed on a meter bar (Figure 3A and Figure S8, Supporting Information). Then, the active AgNWs layer of the device was heated by applying a
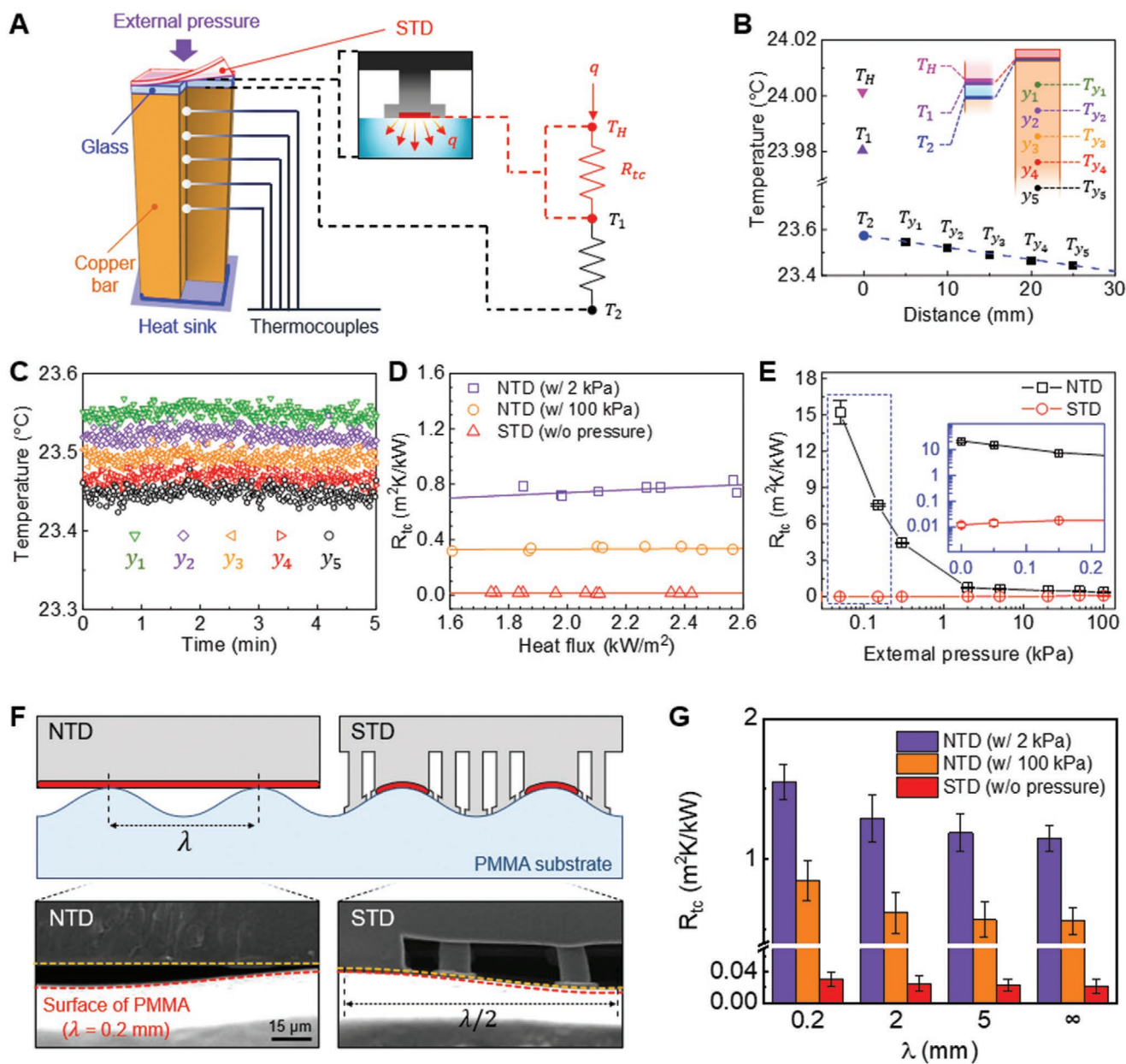
Figure 3. Evaluation of thermal contact resistance of STD. A) Schematic illustration showing the experimental setup for the TCR measurement of the STD. B) Temperature distribution along with the measurement set-up 30 mins after applying a bias voltage of 5 V (input power of 0.25 W). The temperatures at y_1–y_5 were measured with thermocouples installed at 5 mm intervals from the top of the copper bar. C) Steady-state temperatures were measured by the five thermocouples at different positions (y_1–y_5) when a voltage of 5 V (input power of 0.25 W) was applied to the STD for 5 min. D) TCR of the STD and NTD as a function of applied heat flux. E) TCR of the STD and NTD as a function of external pressure for a heat flux of 2.1 kW m^{-2}. F) Mechanical and thermal contact behaviors of the STD and NTD against a non-planar wavy substrate. G) TCR of the STD and NTD on wavy substrates with different wavelengths.
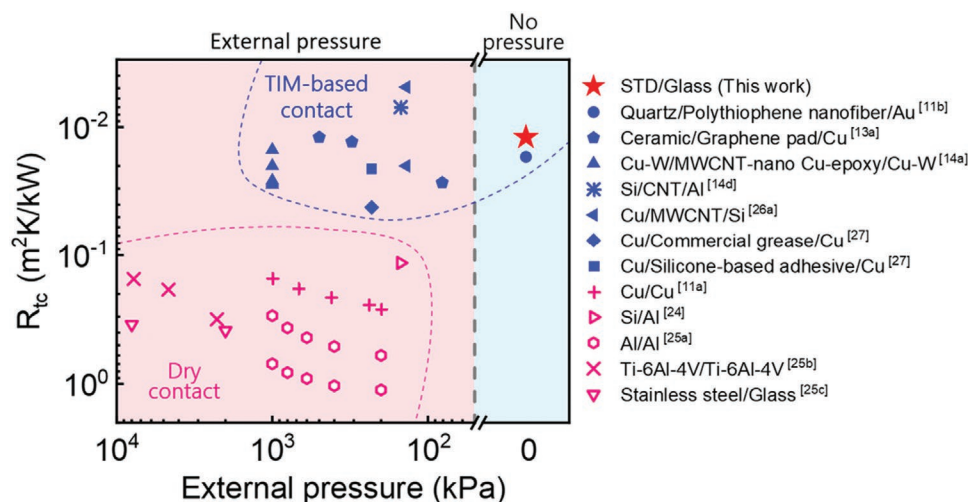
bias voltage of 5 V (power: 0.25 W, heat flux: 2.5 kW m^{-2}) (see Figure S9, Supporting Information and Table S1, Supporting Information for details of the Joule heating experiment). The TCR was calculated using the temperatures of the AgNW-coated side of the thermal device (T_H) and five thermocouples (y_1–y_5) placed at intervals of 5 mm from the top of the copper bar (Figure 3B). The measured steady-state temperature at each position was determined in accordance with ASTM D5470 (the change in temperature was less than ± 0.1 °C over 5 min) and

used to calculate the TCR values (Figure 3C). Under steady-state equilibrium, the temperature (T_1) at the top surface of the glass substrate can be expressed as

$$T_1 = T_2 + \frac{q \times l_{sub}}{k_{sub}} \tag{1}$$

where l_{sub} and k_{sub} represent the thickness and thermal conductivity of the substrate, respectively. T_2 is the surface temperature

ADVANCED
SCIENCE NEWS
www.advancedsciencenews.com

ADVANCED
FUNCTIONAL
MATERIALS
www.afm-journal.de

Figure 4. Comparison of TCR of the STD with TCR of existing dry contact and TIM-based contact.[11a,b,13a,14a,d,24-26a,27]

of the copper bar at the glass-copper interface, which was esti-mated by extrapolating the temperature gradients in the five thermocouples. q is the heat flux due to the resistive heating, which can be obtained using Fourier's law:

$$q = k_{Cu} \frac{\Delta T}{\Delta d} \tag{2}$$

Here, k_{Cu} is the thermal conductivity of the copper bar, and ΔT and Δd are the temperature and position differences inside the copper bar, respectively. The TCR (R_{tc}) between the thermal device and the glass substrate can be then determined using the following equation:

$$R_{tc} = \frac{T_H - T_1}{q} = (T_H - T_1) \frac{\Delta d}{k_{Cu} \Delta T} \tag{3}$$

For comparison, a non-structured flexible thermal device (NTD) on one side of the planar film was coated with AgNWs was utilized as a control. The NTD had the same sheet resist-ance as the STD. Figure 3D shows the calculated TCR values of the STD and NTD as functions of the applied heat flux at dif-ferent applied loads. Under a slight external pressure of 2 kPa, the NTD showed high R_{tc} values of 0.72–0.83 m^2 K kW^{-1} for heat fluxes ranging from 1.6–2.6 kW m^{-2}. When the applied pres-sure increased to 100 kPa, R_{tc} was reduced to 0.35 m^2 K kW^{-1} for all heat flux values. In contrast, the STD exhibited a much lower R_{tc} of 0.012 m^2 K kW^{-1} for the given heat flux values after applying a preload of 2 kPa, even without applying any external loads. Figure 3E shows the measured TCR values of the two devices as functions of the external pressure for a constant heat flux of 2.1 kW m^{-2}. The R_{tc} of the NTD increased rapidly from 0.35 to 15.2 m^2 K kW^{-1} when the external pressure was reduced from 100 to 0.05 kPa. In comparison, the STD maintained a low R_{tc} of approximately 0.01 m^2 K kW^{-1} regardless of the external pressure. This demonstrates the outstanding mechan-ical self-attachment and thermal transport performance of the STD.

In addition to the flat glass substrate, we also measured the R_{tc} of the STD and NTD on rough PMMA substrates with wavy

grooves (Figure 3F). The wavy patterns on the PMMA substrates had an amplitude of 5 μm and four different wavelengths (λ) comprising 0.2, 2, 5, and ∞ mm. Figure 3F (bottom) shows the SEM images of the two devices over the patterned PMMA sub-strate. As shown, the NTD (left) could not make a conformal con-tact with the rough substrate, whereas the STD (right) formed a seamless and intimate contact with the substrate. The adhe-sion strengths of the STD against a flat PMMA substrate were overall similar to those against a flat glass substrate (Figure S10, Supporting Information). Figure 3G shows the measured R_{tc} as a function of the pattern wavelength. For the flat PMMA substrate ($\lambda = \infty$), the TCR values of the NTD were 1.15 and 0.56 m^2 K kW^{-1} under the external pressures of 2 and 100 kPa, respectively. In contrast, the STD exhibited a much lower TCR of 0.02 m^2 K kW^{-1} compared to that of the NTD, even without pressure. The difference in the thermal transport performance between the two devices was more pronounced on rougher substrates. With a decrease in the pattern wavelength from 5 to 0.2 mm (increase in the substrate roughness), the R_{tc} of the NTD increased under the pressures of 2 and 100 kPa. For the rough PMMA substrate with the wavelength of 0.2 mm, R_{tc} reached 1.55 and 0.85 m^2 K kW^{-1} at the external pressures of 2 and 100 kPa, respectively. In contrast, the STD could maintain low R_{tc} values of 0.02–0.03 m^2 K kW^{-1} across the entire range of wavelengths.

We benchmarked the TCR of the self-interfacing contact in our device with those of two conventional thermal contact methods (**Figure** 4 and Table S2, Supporting Information), namely, external pressure-mediated dry contact and thermal interface material (TIM)-based contact. In dry contact, two bodies, which are typically Cu, Al, Ti, Si, or glass, are directly contacted without any interfacial materials.[24] Because these materials are rigid and do not have intrinsic adhesion, a large external pressure (10^2–10^4 kPa) needs to be applied to form a conformal contact interface between the two bodies. Despite the high external pres-sure, the dry contact has a relatively large TCR in the range of 0.12–1.11 m^2 K kW^{-1} (Figure 4 and Table S2, Supporting Informat ion).[11a,24–25] The TIM-based contact is a method in which metal-, ceramic-, or carbon-based thermally conductive interfacial mate-rials are utilized to form conformal mechanical contact between

two bodies and eliminate the air voids, and thereby enhance thermal transport.[26] As shown in Figure 4, the TIM-based contacts exhibit low TCR ranging from 0.005 to 0.04 m² K kW⁻¹, which is comparable to that of the STD.[11b,13a,14a,d,26a,27] However, the application of high external pressure is still required for TIM-based contact owing to the lack of adhesive nature of the TIM. Singh et al. reported that a polythiophene nanofiber-based TIM has a low TCR once the TIM is in contact with a body without the need for external pressure.[11b] However, an initial pressure of 200 kPa has to be applied to the TIM for 10 h to achieve stable adhesion to the body. In contrast to the existing thermal contact methods, our STD is able to form efficient pathways for heat flow against both planar and nonplanar target substrates with minimal TCR without applying high pressure or chemical treatment in an immediate and simple manner.

2.3. Application of the Self-Interfacing Flexible Thermal Device: A Flexible Transparent Heater

Flexible transparent heaters have attracted much attention recently because of their high mechanical flexibility, optical transparency, and applicability to non-planar surfaces.[28] These properties enable a variety of emerging applications, which include smart windows,[29] thermotherapy,[4c] and personal thermal management.[15a] A transparent flexible heater should form a conformal mechanical contact with the target substrate, which may be nonplanar or curved, so that the heat generated from the heater can be efficiently transported to the entire surface of the substrate with minimal energy loss.[4b] To evaluate the thermal transport performance of the flexible resistive heater, we applied the STD to a curved substrate with a bending radius of 10 mm (**Figure 5**A). An AgNW-coated planar PET film (NTD), which is a typical example of an existing flexible heater, was used as a control. The NTD was attached to the curved substrate using polyimide tape, while the STD was attached to the substrate via self-adhesion. Both heaters were 100 μm thick. The cross-sectional temperature gradients of the heaters were measured by infrared (IR) thermography while a DC voltage of 5 V was applied. After 5 min of voltage application, the surface temperature of the curved substrate in contact with the STD heater reached 52.5 °C. This value is identical to the surface temperature of the STD heater and indicates a negligible temperature
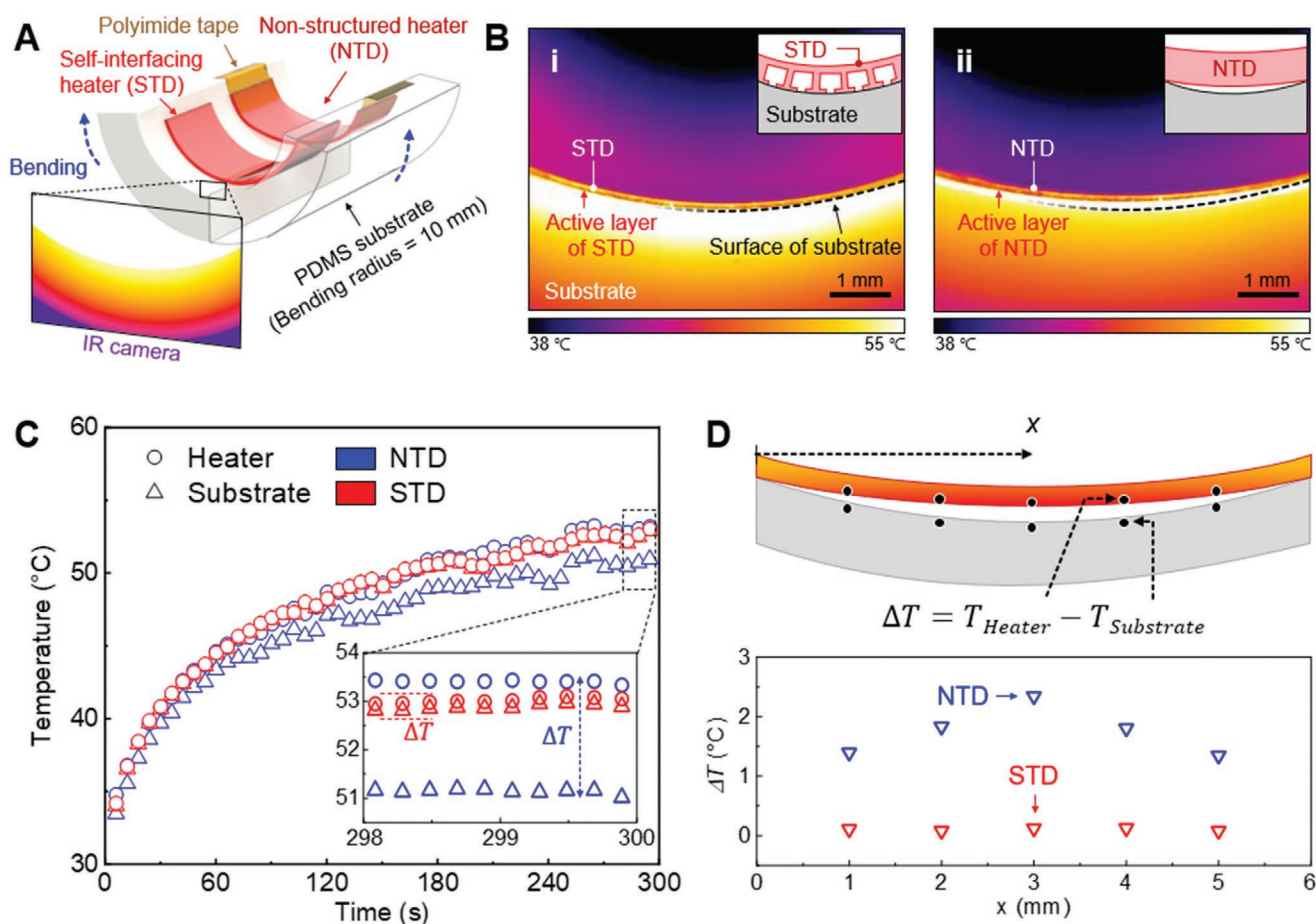
Figure 5. Application of the STD as a flexible transparent heater. A) Conceptual illustration showing the STD and NTD applied on a curved substrate with a bending radius of 10 mm. The cross-sectional temperature gradients of the heaters and substrates were examined by IR thermography while a DC voltage of 5 V (input power of 0.25 W) was applied. B) IR thermography images of the (i) STD and (ii) NTD on the curved substrate after 5 min of voltage application. C) Surface temperatures of the thermal devices (STD and NTD) and the curved substrate as functions of the voltage application time. D) Temperature difference between the surfaces of the thermal devices (STD and NTD) and the substrate at different horizontal positions after applying a voltage of 5 V for 5 min.

difference between the heater and the substrate (Figure 5B-i, 5C, and Figure S11, Supporting Information). In addition, the surface temperature of the curved substrate was uniform across the surface (Figure 5B -i). These results demonstrate that the self-interfacing heater has high heat transfer capability with minimal heat loss even on a curved substrate. In contrast, the surface temperature of the curved substrate in contact with the NTD heater was noticeably lower than that of the heater (50.9 °C) and not uniform across the substrate (Figure 5B -ii and 5C). For example, the temperatures of the substrate at the center ($x = 3$ mm in Figure 5D) and side locations ($x = 1$ or 5 mm) were 2.3 and 1.3 °C lower than the surface temperature of the heater (Figure 5B–D). This is because the AgNW-coated side of the non-structured flexible heater could not form close conformal contact with the substrates owing to the roughness and non-adhesiveness of the AgNWs even when adhesive tapes were used. We also investigated the Joule-heating behavior of the STD heater during repeated power-on and off cycles (bias voltage of 5 V, input power of 0.25 W). The STD heater could maintain stable heating performance for 10 repeated heating/cooling cycles (Figure S12, Supporting Information).

3. Conclusion

In summary, we proposed a self-interfacing flexible thermal device which can minimize heat loss at the contact interface by maximizing the vdW coupling at the interface through an integrated design of percolating AgNW thermal networks and bioinspired adhesive architectures. The STD achieved the maximum adhesion strength of 538.9 kPa and a low TCR of 0.012 m^2 K kW^{-1} without the application of external pressure or the use of surface chemistries. Thus, it can efficiently and uniformly transfer heat to planar or curved substrates. The TCR of the self-interfacing device can potentially be reduced further by incorporating other conducting nanomaterials (e.g., graphene) or surface chemistries (e.g., self-assembled monolayers) into the device.[2b,30] Anisotropic heat transfer properties can also be realized in the self-interfacing device by utilizing aligned nanosheets (e.g., boron nitride nanosheet).[13b] The proposed STD device is expected to exhibit limited heat transfer performance at higher temperatures above ≈150 °C because AgNWs used in the STD device are thermally oxidized above such high temperatures. The STD device also showed limited adhesion strengths against rough surfaces with high root mean square (RMS) values (e.g., textiles). In addition, scalable fabrication methods for the STD need to be further explored. Nonetheless, we expect that the STD, with its low TCR, strong self-attachability, mechanical flexibility, and optical transparency, can contribute to the development of advanced thermal transport devices with dynamic and highly non-uniform surfaces, which include smart windows, flexible heaters, wearable thermotherapy, thermal haptics, and energy devices.

4. Experimental Section

Fabrication of the Self-Interfacing Flexible Thermal Device: The fabrication procedure of the STD includes photolithography, selective coating of AgNWs, and UV molding (Figure 2A and Figure S1, Supporting Information). The detailed steps are as follows: The master mold with the negative pattern of the grids and pillars with tips was prepared on a Si wafer through photolithography.[21] A lift-off resist (LOR 30 B, Microchem Corp., USA) and a photoresist (SU-8 3010, Microchem Corp., USA) were individually spin-coated on a dehydrated Si wafer to form a bilayer. Each spin-coating step was followed by a soft-baking process (30 min baking at 200 °C for the LOR layer, 10 min baking at 95 °C for the SU-8 layer). The negative grid and pillar pattern in the SU-8 layer were produced through photomask-based selective UV exposure ($\lambda = 365$ nm, dose = 250 mJ cm^{-2}) followed by development using an SU-8 developer (Microchem Corp., USA) for 5 min. Subsequently, a LOR developer (AZ 400 K, AZ Electronics Materials Corp., USA) was utilized to selectively form a 2 µm-long undercut on the LOR layer at the bottom of the grid and pillar pattern. Then, AgNW solution (Flexio Corp., Republic of Korea) was deposited on the fabricated master mold, in which the undercut of the patterns enabled selective deposition of the AgNWs. The purchased solution contained 0.1 wt% AgNWs (20 nm diameter and 20 µm length) dispersed in DI water. After deposition, the AgNW-coated master mold was dried at 70 °C for 1 h to remove the remaining solvent. The unwanted AgNW layer on the top surface of the master mold outside the trench of the patterns was selectively peeled off using a commercial adhesive tape. Subsequently, an e-PUA solution mixed with 10 wt% Triton X-100 (Sigma-Aldrich, USA) was poured over the master mold.[31] The dispensed e-PUA solution was covered with a PET film and crosslinked for 30 min by UV irradiation ($\lambda = 365$ nm, dose = 300 mJ cm^{-2}). Finally, the crosslinked e-PUA film with microstructures and selectively coated AgNWs was removed from the master mold to yield the STD.

Surface Characterization: SEM and EDS images of the enlarged microstructures of the STD were obtained using a scanning electron microscope (Quanta 200 FEG, FEI, USA). For imaging, a 5 nm-thick Pt layer was sputtered on the surface of the SEM samples. Real-time images of the temperature distribution were captured using an IR microscope system (A325SC, FLIR Systems AB, Sweden). For the measurements, samples with a sheet resistance of ≈20 Ω sq^{-1} were utilized.

Measurement of Adhesion Strength: The adhesion strength of the STD was measured using a custom-built adhesion tester, which consisted of two parts, namely, a lower part (fixed substrate) and an upper part (vertically movable jig). STD samples (area: 1 × 1 cm^2) were mounted on the horizontal surface of the upper part with the samples facing down. During the measurement, the samples were brought into contact with the flat glass substrate fixed on the bottom part with a downward preload of controlled magnitude and duration. Then, a pulling force in the upward direction was applied until the samples were detached from the substrates (pulling rate: 1 mm s^{-1}). During the test cycle, the applied loads were collected through a load cell (KTOYO, Republic of Korea) connected to the upper part of the equipment, and each test was repeated ten times.

Analysis of Optical and Electrical Properties: The optical transmittance was obtained using a UV–Vis-NIR spectrophotometer (Cary 5000, Agilent, USA) over the wavelength range of 400–800 nm. The sheet resistance was measured using the four-point probe method with a surface resistivity meter (CMT-SR1000N, Advanced Instrument Technology, Republic of Korea).

Measurement of Thermal Contact Resistance: The TCR was measured using a steady-state method based on the ASTM Standard D5470. The meter bar made of copper (thermal conductivity: 380 W m^{-1} K^{-1}) was 50 mm high and had a square section of 10 mm side length. To measure the TCR during the heating of the STDs, a thin electrically insulating layer (thickness: 0.17 mm) of glass (thermal conductivity: 0.83 W m^{-1} K^{-1}) was attached to the top surface of the meter bar. In addition, to measure the TCR on rough surfaces, PMMA film (thermal conductivity: 0.24 W m^{-1} K^{-1}) was applied via an aluminum mold-based hot-pressing process (1 MPa, 140 °C for 3 min) and used in place of the glass substrate. The STD sample connected to a power generator was then attached to the top surface of the glass with the samples facing down. To measure the temperature gradient of the meter bar,

**ADVANCED
SCIENCE NEWS**

www.advancedsciencenews.com

**ADVANCED
FUNCTIONAL
MATERIALS**

www.afm-journal.de

five thermocouples (*K*-type) were inserted into the center of the copper bar through five holes (1.2 mm diameter) located at intervals of 5 mm from the top surface. The air gaps in the holes were removed by inserting thermocouples with thermal grease (Loctite TG100, Henkel, Germany). A heat sink was installed at the bottom of the copper bar for heat dissipation, and the measurement system was thermally insulated from convection and radiation using glass wool and an extruded polystyrene foam board. Real-time data of the temperatures of the meter bar and the STD were collected via thermocouples connected to the source measurement equipment (DAQ970A, KEYSIGHT, USA).

Supporting Information

Acknowledgements

Conflict of Interest

The authors declare no conflict of interest.

Data Availability Statement

The data that support the findings of this study are available from the corresponding author upon reasonable request.

Keywords

[1] E. T. Swartz, R. O. Pohl, *Rev. Mod. Phys.* **1989**, *61*, 605.

[2] a) M. G. Cooper, B. B. Mikic, M. M. Yovanovich, *Int. J. Heat Mass Transfer* **1969**, *12*, 279; b) M. D. Losego, M. E. Grady, N. R. Sottos, D. G. Cahill, P. V. Braun, *Nat. Mater.* **2012**, *11*, 502.

[3] M. Hu, X. Zhang, D. Poulikakos, C. P. Grigoropoulos, *Int. J. Heat Mass Transfer* **2011**, *54*, 5183.

[4] a) A. Hazarika, B. K. Deka, D. Kim, H. E. Jeong, Y.-B. Park, H. W. Park, *Nano Lett.* **2018**, *18*, 6731; b) J. Ahn, J. Gu, B. Hwang, H. Kang, S. Hwang, S. Jeon, J. Jeong, I. Park, *Nanotechnology* **2019**, *30*, 455707; c) J. Jang, J. Kim, H. Shin, Y.-G. Park, B. J. Joo, H. Seo, J.-e. Won, D. W. Kim, C. Y. Lee, H. K. Kim, J.-U. Park, *Sci. Adv.* **2021**, *7*, eabf7194; d) Q. Yan, F. E. Alam, J. Gao, W. Dai, X. Tan, L. Lv, J. Wang, H. Zhang, D. Chen, K. Nishimura, L. Wang, J. Yu, J. Lu, R. Sun, R. Xiang, S. Maruyama, H. Zhang, S. Wu, N. Jiang, C.-T. Lin, *Adv. Funct. Mater.* 2104062, **2021**, https://doi.org/10.1002/adfm.202104062; e) M. Kim, D. Lee, S. Son, Y. Yang, H. Lee, J. Rho,

[5] P. J. O'Brien, S. Shenogin, J. Liu, P. K. Chow, D. Laurencin, P. H. Mutin, M. Yamaguchi, P. Keblinski, G. Ramanath, *Nat. Mater.* **2013**, *12*, 118.

[6] a) S. Majumdar, J. A. Malen, A. J. McGaughey, *Nano Lett.* **2017**, *17*, 220; b) S. Kaur, N. Raravikar, B. A. Helms, R. Prasher, D. F. Ogletree, *Nat. Commun.* **2014**, *5*, 3082; c) H. Ko, H. H. Park, H. Byeon, M. Kang, J. Ryu, H. J. Sung, S. J. Lee, H. E. Jeong, *Sci. Adv.* **2019**, *5*, eaax8935.

[7] F. Sun, T. Zhang, M. M. Jobbins, Z. Guo, X. Zhang, Z. Zheng, D. Tang, S. Ptasinska, T. Luo, *Adv. Mater.* **2014**, *26*, 6093.

[8] H. Fan, M. Wang, D. Han, J. Zhang, J. Zhang, X. Wang, *J. Phys. Chem. C* **2020**, *124*, 16748.

[9] J. Wang, Z. Zhang, R. Shi, B. N. Chandrashekar, N. Shen, H. Song, N. Wang, J. Chen, C. Cheng, *Adv. Mater. Interfaces* **2019**, *7*, 1901582.

[10] a) W. Dai, L. Lv, J. Lu, H. Hou, Q. Yan, F. E. Alam, Y. Li, X. Zeng, J. Yu, Q. Wei, X. Xu, J. Wu, N. Jiang, S. Du, R. Sun, J. Xu, C.-P. Wong, C.-T. Lin, *ACS Nano* **2019**, *13*, 1547; b) B. Gotsmann, M. A. Lantz, *Nat. Mater.* **2013**, *12*, 59.

[11] a) B. Feng, F. Faruque, P. Bao, A.-T. Chien, S. Kumar, G. P. Peterson, *Appl. Phys. Lett.* **2013**, *102*, 093105; b) V. Singh, T. L. Bougher, A. Weathers, Y. Cai, K. Bi, M. T. Pettes, S. A. McMenamin, W. Lv, D. P. Resler, T. R. Gattuso, D. H. Altman, K. H. Sandhage, L. Shi, A. Henry, B. A. Cola, *Nat. Nanotechnol.* **2014**, *9*, 384; c) Y. Jin, C. Shao, J. Kieffer, K. P. Pipe, M. Shtein, *J. Appl. Phys.* **2012**, *112*, 093503.

[12] a) G. T. Hohensee, R. B. Wilson, D. G. Cahill, *Nat. Commun.* **2015**, *6*, 6578; b) A. M. Hofmeister, *Proc. Natl. Acad. Sci. USA* **2007**, *104*, 9192; c) W. G. Bae, H. Ko, J. Y. So, H. Yi, C. H. Lee, D. H. Lee, Y. Ahn, S. H. Lee, K. Lee, J. Jun, H. H. Kim, N. L. Jeon, W. Jung, C. S. Song, T. Kim, Y. C. Kim, H. E. Jeong, *Sci. Transl. Med.* **2019**, *11*, eaaw3329.

[13] a) W. Dai, T. Ma, Q. Yan, J. Gao, X. Tan, L. Lv, H. Hou, Q. Wei, J. Yu, J. Wu, Y. Yao, S. Du, R. Sun, N. Jiang, Y. Wang, J. Kong, C. Wong, S. Maruyama, C.-T. Lin, *ACS Nano* **2019**, *13*, 11561; b) H. Hong, Y. H. Jung, J. S. Lee, C. Jeong, J. U. Kim, S. Lee, H. Ryu, H. Kim, Z. Ma, T.-i. Kim, *Adv. Funct. Mater.* **2019**, *29*, 1902575.

[14] a) P. Zhang, Q. Li, Y. Xuan, *Compos. Pt. A-Appl. Sci. Manuf.* **2014**, *57*, 1; b) Y. Zhou, S. Wu, Y. Long, P. Zhu, F. Wu, F. Liu, V. Murugadoss, W. Winchester, A. Nautiyal, Z. Wang, Z. Guo, *ES Mater. Manuf.* **2020**, *7*, 4; c) J. P. Gwinn, R. L. Webb, *Microelectron. J.* **2003**, *34*, 215; d) K. Zhang, Y. Chai, M. M. F. Yuen, D. G. W. Xiao, P. C. H. Chan, *Nanotechnology* **2008**, *19*, 215706.

[15] a) S. Hong, H. Lee, J. Lee, J. Kwon, S. Han, Y. D. Suh, H. Cho, J. Shin, J. Yeo, S. H. Ko, *Adv. Mater.* **2015**, *27*, 4744; b) X. Chen, S. Nie, W. Guo, F. Fei, W. Su, W. Gu, Z. Cui, *Adv. Electron. Mater.* **2019**, *5*, 1800991; c) H. Li, C. S. L. Koh, Y. H. Lee, Y. Zhang, G. C. Phan-Quang, C. Zhu, Z. Liu, Z. Chen, H. Y. F. Sim, C. L. Lay, Q. An, X. Y. Ling, *Nano Energy* **2020**, *73*, 104723; d) C. Zhu, A. Chortos, Y. Wang, R. Pfattner, T. Lei, A. C. Hinckley, I. Pochorovski, X. Yan, J. W.-F. To, J. Y. Oh, J. B.-H. Tok, Z. Bao, B. Murmann, *Nat. Electron.* **2018**, *1*, 183; e) Z. Niu, F. Cui, E. Kuttner, C. Xie, H. Chen, Y. Sun, A. Dehestani, K. Schierle-Arndt, P. Yang, *Nano Lett.* **2018**, *18*, 5329; f) D.-H. Kim, N. Lu, R. Ma, Y.-S. Kim, R.-H. Kim, S. Wang, J. Wu, S. M. Won, H. Tao, A. Islam, K. J. Yu, T.-i. Kim, R. Chowdhury, M. Ying, L. Xu, M. Li, H.-J. Chung, H. Keum, M. McCormick, P. Liu, Y.-W. Zhang, F. G. Omenetto, Y. Huang, T. Coleman, J. A. Rogers, *Science* **2011**, *333*, 838.

[16] a) Y. Cho, G. Kim, Y. Cho, S. Y. Lee, H. Minsky, K. T. Turner, D. S. Gianola, S. Yang, *Adv. Mater.* **2015**, *27*, 7788; b) S. Gorb, M. Varenberg, A. Peressadko, J. Tuma, *J. R. Soc., Interface* **2007**, *4*, 271; c) H. E. Jeong, J.-K. Lee, H. N. Kim, S. H. Moon, K. Y. Suh, *Proc.*

Natl. Acad. Sci. USA **2009**, *106*, 5639; d) D.-M. Drotlef, M. Amjadi, M. Yunusa, M. Sitti, *Adv. Mater.* **2017**, *29*, 1701353; e) K. Autumn, Y. A. Liang, S. T. Hsieh, W. Zesch, W. P. Chan, T. W. Kenny, R. Fearing, R. J. Full, *Nature* **2000**, *405*, 681; f) E. Arzt, S. Gorb, R. Spolenak, *Proc. Natl. Acad. Sci. USA* **2003**, *100*, 10603; g) A. del Campo, C. Greiner, I. Álvarez, E. Arzt, *Adv. Mater.* **2007**, *19*, 1973; h) H. Yi, S.-H. Lee, H. Ko, D. Lee, W.-G. Bae, T.-i. Kim, D. S. Hwang, H. E. Jeong, *Adv. Funct. Mater.* **2019**, *29*, 1902720; i) C. Son, S. Kim, *ACS Appl. Mater. Interfaces* **2021**, *13*, 27656.

[17] a) A. J. Marsden, D. G. Papageorgiou, C. Vallés, A. Liscio, V. Palermo, M. A. Bissett, R. J. Young, I. A. Kinloch, *2D Mater.* **2018**, *5*, 032003; b) H. Wang, K. Kurata, T. Fukunaga, H. Ago, H. Takamatsu, X. Zhang, T. Ikuta, K. Takahashi, T. Nishiyama, Y. Takata, *J. Appl. Phys.* **2016**, *119*, 244306; c) Y. Zhao, M. L. Fitzgerald, Y. Tao, Z. Pan, G. Sauti, D. Xu, Y. Q. Xu, D. Li, *Nano Lett.* **2020**, *20*, 7389; d) T. W. Ebbesen, H. J. Lezec, H. Hiura, J. W. Bennett, H. F. Ghaemi, T. Thio, *Nature* **1996**, *382*, 54.

[18] a) T.-G. Kim, C.-W. Park, D.-Y. Woo, J. Choi, S. S. Yoon, *Appl. Therm. Eng.* **2020**, *165*, 114572; b) S. Chen, Q. Wu, C. Mishra, J. Kang, H. Zhang, K. Cho, W. Cai, A. A. Balandin, R. S. Ruoff, *Nat. Mater.* **2012**, *11*, 203; c) M. Fujii, X. Zhang, H. Xie, H. Ago, K. Takahashi, T. Ikuta, H. Abe, T. Shimizu, *Phys. Rev. Lett.* **2005**, *95*, 065502.

[19] Y. Park, J. Shim, S. Jeong, G. R. Yi, H. Chae, J. W. Bae, S. O. Kim, C. Pang, *Adv. Mater.* **2017**, *29*, 1606453.

[20] F. Suarez, A. Nozariasbmarz, D. Vashaee, M. C. Öztürk, *Energy Environ. Sci.* **2016**, *9*, 2099.

[21] H. Yi, M. Kang, M. K. Kwak, H. E. Jeong, *ACS Appl. Mater. Interfaces* **2016**, *8*, 22671.

[22] T. Deng, K. K. Varanasi, M. Hsu, N. Bhate, C. Keimel, J. Stein, M. Blohm, *Appl. Phys. Lett.* **2009**, *94*, 133109.

[23] M. Seong, I. Hwang, J. Lee, H. E. Jeong, *Sensors* **2020**, *20*, 6965.

[24] Z. L. Gao, K. Zhang, M. M. Yuen, *Nanotechnology* **2011**, *22*, 265611.

[25] a) J.-W. Zhao, R. Zhao, Y.-K. Huo, W.-L. Cheng, *Int. J. Heat Mass Transfer* **2019**, *140*, 705; b) J.-J. Gou, X.-J. Ren, Y.-J. Dai, S. Li, W.-Q. Tao, *Comput. Fluids* **2018**, *164*, 2; c) A. T. Vu, T. Helmig, A. N. Vu, Y. Frekers, T. Grunwald, R. Kneer, T. Bergs, *J. Am. Ceram. Soc.* **2019**, *103*, 1258.

[26] a) J. H. Taphouse, O. N. L. Smith, S. R. Marder, B. A. Cola, *Adv. Funct. Mater.* **2014**, *24*, 465; b) W. Zhang, Q.-Q. Kong, Z. Tao, J. Wei, L. Xie, X. Cui, C.-M. Chen, *Adv. Mater. Interfaces* **2019**, *6*, 1900147.

[27] X. Zhang, K. K. Yeung, Z. Gao, J. Li, H. Sun, H. Xu, K. Zhang, M. Zhang, Z. Chen, M. M. F. Yuen, S. Yang, *Carbon* **2014**, *66*, 201.

[28] D. T. Papanastasiou, A. Schultheiss, D. Muñoz-Rojas, C. Celle, A. Carella, J. P. Simonato, D. Bellet, *Adv. Funct. Mater.* **2020**, *30*, 1910225.

[29] L. Veeramuthu, B.-Y. Chen, C.-Y. Tsai, F.-C. Liang, M. Venkatesan, D.-H. Jiang, C.-W. Chen, X. Cai, C.-C. Kuo, *RSC Adv.* **2019**, *9*, 35786.

[30] A. G. Ricciardulli, S. Yang, G.-J. A. H. Wetzelaer, X. Feng, P. W. M. Blom, *Adv. Funct. Mater.* **2018**, *28*, 1706010.

[31] I. Hwang, M. Seong, H. Yi, H. Ko, H.-H. Park, J. Yeo, W.-G. Bae, H. W. Park, H. E. Jeong, *Adv. Funct. Mater.* **2020**, *30*, 2000458.